Sensors & Actuators: B. Chemical 454 (2026) 139621

Contents lists available at ScienceDirect

Sensors and Actuators: B. Chemical

journal homepage: www.elsevier.com/locate/snb

A session-lasting biostable and biocompatible hydrogel microneedle patch for nanozyme-mediated on-site and smartphone-based quantification of skin H_2O_2

Sihui Wang [a,1], Feng Liu [c,1], Meng Sun [a], Hongchun Gu [a], Lei Yang [c,*], Xun Feng [b,**], Yang Chen [a,***]

[a] Department of Pharmaceutics, School of Pharmacy, China Medical University, Shenyang 110122, China
[b] Department of Sanitary Chemistry, School of Public Health, Shenyang Medical College, Shenyang 110034, China
[c] NMPA Key Laboratory for Technical Research on Drug Products in Vitro and in Vivo Correlation, Sichuan Institute for Drug Control, Chengdu 611731, China

ARTICLE INFO

Keywords:
Hydrogen peroxide
Nanozyme
Microneedle
Biostable
Biocompatible

ABSTRACT

Hydrogen peroxide (H_2O_2) in skin tissue serves as a critical biomarker for oxidative stress and physiological status, yet its precise in situ monitoring remains challenging due to the lack of non-invasive, real-time sensing platforms. Herein, we presented a smartphone-assisted biosensing system based on a nanozyme-integrated hydrogel microneedle patch for on-site and quantitative detection of cutaneous H_2O_2. The sensing platform incorporated a palladium-embedded metal-organic framework (Pd-PCN) with enhanced peroxidase-like activity, which was co-immobilized with a chromogenic substrate in a polymeric composite hydrogel microneedle array. This composite matrix maintained structural integrity and biocompatibility during short-term skin application while providing an aqueous microenvironment favorable for nanozyme-catalyzed reactions. Upon insertion into the skin, H_2O_2 from interstitial fluid would diffuse into the microneedle and trigger a colorimetric reaction. The resulting color intensity could be quantitatively captured via smartphone-based RGB analysis. The system demonstrated a wide linear detection range (5–100 μM), a low detection limit (1.53 μM), high reproducibility (RSD < 5 %), and negligible interference from common biological substances. Confocal imaging and mechanical testing further confirm the structural stability and skin-penetration capability of the microneedle under operational conditions. This work established a reliable, minimally invasive, and user-friendly platform for continuous monitoring of oxidative biomarkers in skin, paving the way for personalized dermatological care and point-of-care diagnostics.

1. Introduction

In the skin, hydrogen peroxide (H_2O_2) serves as both a crucial mobile signaling molecule and a driver of oxidative stress through direct oxidation and radical generation [1]. Elevated levels of H_2O_2 are a common characteristic for cutaneous disorders like vitiligo and skin epithelioma, confirming its status as a key pathological biomarker [2]. Therefore, accurate and on-site quantification of cutaneous H_2O_2 dynamics is critical for elucidating disease mechanisms and guiding therapy.

Conventional H_2O_2 detection techniques (e.g., chromatography, fluorogenic assay, and electroanalysis) rely on invasive sampling and *ex vivo* analysis, making them complex, time-consuming, and unsuitable for continuous monitoring. Furthermore, their invasiveness raises concerns regarding patient discomfort and infection risk [3]. Therefore, developing a sensing platform capable of non-invasive and in-situ monitoring

* Correspondence to: NMPA Key Laboratory for Technical Research on Drug Products in Vitro and in Vivo Correlation, Sichuan Institute for Drug Control, NO. 8 Xinwen Road, High-tech zone, Chengdu 611731, PR China.
** Correspondence to: Department of Sanitary Inspection, School of Public Health, Shenyang Medical College, No.146 Yellow River North Street, Yuhong District, Shenyang 110034, China.
*** Correspondence to: Department of Pharmaceutics, School of Pharmacy, China Medical University, No.77 Puhe Road, Shenyang North New Area, Shenyang 110122, China.
E-mail addresses: 1504868330@qq.com (L. Yang), fengxundfx@163.com (X. Feng), chenyangpharm@163.com (Y. Chen).
[1] Contribute equally to this work.

https://doi.org/10.1016/j.snb.2026.139621
Received 11 November 2025; Received in revised form 17 January 2026; Accepted 5 February 2026
Available online 7 February 2026

of H_2O_2 remains a critical unmet challenge.

To this end, a fast and reliable signal transduction mechanism is paramount. Nanozymes, nanomaterials mimicking the catalytic functions of natural enzymes, have emerged as a robust approach [4]. In particular, peroxidase (POD)-mimicking nanozymes can catalyze the oxidation of chromogenic substrates in the presence of H_2O_2, generating a distinct colorimetric signal quantifiable via smartphone camera [5]. This capability makes them powerful molecular transducers, converting localized H_2O_2 levels into an optical readout for point-of-care application [6]. Among various nanozymes, palladium (Pd) nanoparticles are renowned for their exceptionally high POD-like activity [7]. However, their tendency to aggregate compromises catalytic stability and hinders practical application [8]. A promising strategy to overcome this limitation is to stabilize Pd nanoparticles within a robust porous scaffold. This study employed porous coordination network-224 (PCN-224), a porphyrin-based zirconium metal-organic framework (MOF), which our prior work established as a safe and effective cutaneous carrier [9,10]. Owing to their well-defined pores, a fundamental property of MOFs [11], PCN-224 are expected not only to confine and stabilize Pd nanoparticles against aggregation but also to enhance their catalytic performance synergistically, yielding the highly active and stable composite nanozyme, Pd-PCN.

For skin application, such nanozyme sensors requires a minimally invasive platform to bypass the cutaneous barrier. In this context, microneedle (MN) arrays have emerged as a highly promising approach [12]. While nanozyme-based MNs are well-established for therapy [13], their application in sensing represents an emerging field. Current colorimetric MN sensors mostly rely on oxidase-like nanozymes to analyze reducing agents or on hybrid systems with natural enzymes to analyze specific molecules such as glucose [14,15]. However, employing POD-mimicking nanozymes in MN sensors typically introduces compositional complexity brought by the multi-component reaction system, resulting in a decoupled architecture where the MN serves only for sampling or delivery [16,17]. This separation thus hinders the development of a fully integrated and *in-situ* platform. Here, we demonstrate an integrated system (Pd-PCN/TMB@MN) that co-immobilizes a POD-mimic Pd-PCN and TMB within a single MN matrix for direct H_2O_2 detection. Unlike reported cutaneous H_2O_2 MN sensors based on electrochemistry (exemplified by a system integrating hollow MNs with a Prussian blue/carbon nanotube composite electrode) [18], our work focuses on a colorimetric sensing strategy. A key challenge thus lie in the development of an all-in-one MN matrix that guarantees both stable signal acquisition and excellent biocompatibility throughout the measurement period.

Herein, we engineered a session-lasting (i.e., maintaining integrity throughout the period from application to removal) hydrogel MN patch. The Pd-PCN nanozymes and chromogenic substrate TMB were sequentially incorporated into its matrix, ensuring structural integrity and biocompatibility during use. The MNs create transient microchannels in the skin. Upon hydration, the swollen matrix provided an optimal aqueous microenvironment, where the diffused H_2O_2 triggered a nanozyme-catalyzed colorimetric reaction with TMB, yielding a localized blue signal. This signal was captured in real time via a smartphone camera and quantitatively analyzed via RGB analysis, offering a reliable platform for on-site H_2O_2 monitoring.

2. Materials and methods

2.1. Materials

Zirconyl chloride octahydrate ($ZrOCl_2.8H_2O$, 99 %), benzoic acid (BA, 99.5 %), palladium (II) chloride ($PdCl_2$, Pd $\geq$ 59.0 %, ethylene glycol (98 %), meso-tetra (4-carboxyphenyl) porphine (TCPP, dry content 75 %) were all purchased from Aladdin Reagents Co. Ltd (Shanghai, China). 3,3,5,5-Tetramethylbenzidine (TMB, 98 %) and poly(vinyl alcohol) (PVA, 99 %) were obtained from Rhawn Chemical Reagent Co., Ltd. (Shanghai, China). Chitosan (CS) was supplied by Shanghai Macklin Biochemical Co., Ltd. (Shanghai, China). All chemicals and reagents were of at least analytical reagent grade. Porcine skin was obtained from Jingde Agricultural Products Co., Ltd. (Xingtai, China).

2.2. Preparation and characterization of Pd-PCN

Spherical PCN-224 nanoparticles were prepared according to our previous report [10]. Briefly, a mixture of 100 mg TCPP, 3.3 g BA, and 300 mg $ZrOCl_2{\cdot}8H_2O$ in 100 mL N, N-dimethylformamide (DMF) was ultrasonicated until dissolved. The solution was then stirred at 250 rpm and heated at 90 ℃ for 6 h. The resulting precipitate was collected by centrifugation (14,000 rpm, 30 min, 4 ℃), washed sequentially with DMF and anhydrous ethanol, and finally lyophilized for 12 h to obtain a purplish-red powder, which was stored protected from light.

Subsequently, Pd nanoparticles were loaded via an in-situ reduction method. The PCN-224 of 100 mg was uniformly dispersed in 100 mL of ethylene glycol. The dispersion was stirred at 250 rpm and heated at 90 °C for 15 min. Then, a solution of $PdCl_2$ (60 mg in 4 mL of ethylene glycol) was added dropwise, and the reaction was allowed to proceed under the same conditions for 7 h. The product (Pd-PCN) was collected by centrifugation (12,000 rpm, 30 min), washed thoroughly with ethanol and ultrapure water, and freeze-dried. Residual DMF was analyzed via gas chromatography (GC) and confirmed to be at a negligible level.

The morphologies, crystal structures, and molecular information were characterized using scanning electron microscopy (SEM, Zeiss Gemini 300, Germany), transmission electron microscopy (TEM, Talos F200X, Thermo Fisher, USA), X-ray diffraction (XRD, Bruker D8 advance, Germany), and Fourier-transform infrared spectroscopy (FTIR, IS50, Thermo Fisher, USA).

2.3. Evaluation of the POD-like activity

The POD-like activity was evaluated in a TMB-H_2O_2 system. For each test, 10 μL Pd-PCN dispersion (1 mg/mL), 100 μL H_2O_2 solution (0.1 M), and 50 μL TMB solution (10 mM) were sequentially introduced into 2 mL sodium acetate buffer (0.2 M, pH 4.0). After reaction for 20 min, the absorbance at 652 nm was measured using a UV-Vis spectrophotometer (UV-4802S, UNICO, China). Activities of the Pd-PCN, pristine PCN-224 and a blank control was compared. Optimal conditions were determined by varying either H_2O_2 concentration or reaction temperature.

Under the optimized conditions, the time-dependent absorbance was recorded at 1-min intervals to establish the reaction kinetic profile. The Michaelis constant (K_m) was calculated from this curve.

The catalytic stability was assessed by testing Pd-PCN (1 mg/mL) from different batches. The specificity was verified by measuring absorption in the presence of various interfering substances.

2.4. Preparation and characterization of Pd-PCN/TMB@MN

Precursor solutions were prepared by co-dissolving PVA and CS in aqueous acetic acid (0.1 M, pH 4.0) at varying concentration ratios. Then, 1 mL of the solution was cast into a polydimethylsiloxane (PDMS) mold, followed by centrifugation, drying, and demolding. The resulting MNs were evaluated under a microscope (BDS400, CNOPTEC, China) based on three key parameters, including needle yield (defined as number of intact needles divided by the total number of needles), the number of penetrated Parafilm™ layers, and the insertion efficiency (defined as number of holes in the specific Parafilm™ layer divided by total number of needles).

The Pd-PCN/TMB@MN was then fabricated using a sequential loading method. The optimal precursor solution was first cast onto the PDMS mold. Then, 10 μL of the Pd-PCN nanozyme dispersion (1 mg/mL) was added and centrifuged (3500 rpm, 30 min) to sequester the nanozyme in the needle tips. Following that, 100 μL of TMB solution (10 mM)

was introduced and centrifuged (3000 rpm, 30 min) into the matrix. After drying and demolding, the Pd-PCN/TMB@MN patch was obtained.

The MN morphology was characterized by SEM (Zeiss Gemini 300, Germany). The mechanical property was tested using a texture analyzer (Universal TA, Shtengba, China) at 0.05 mm/s, generating compressive load-displacement curves.

2.5. Biocompatibility study

The cytocompatibility was assessed on human immortalized keratinocyte cell line (HaCaT) via the CCK-8 assay. Cells were seeded in a 96-well plate at a density of 10,000 cells/well and pre-cultured for 24 h (37°C, 5 % CO_2) to allow attachment. To simulate the physiological interface *in vivo* where the acidic MN encountered neutral interstitial fluid, the test was conducted in neutral complete culture medium. An extract of the Pd-PCN/TMB@MN patches was prepared by incubation in this medium for 24 h to obtain a physiologically relevant extract with the original concentration of 0.068 g/mL, and then serially diluted (3400–13.28 μg/mL) for testing. Separately, the Pd-PCN nanoparticles were directly dispersed and diluted in the same medium (100–0.39 μg/mL). Cells were treated with these samples for 24 h. Thereafter, 10 % (v/v) CCK-8 solution was added, followed by incubation for 20 min. The absorbance (OD value) at 450 nm was measured for each well. Cells cultured in medium without any extract served as the blank control. The cell viability was calculated according to the following formula:

$$Cell\ Viability(\%) = \frac{(OD_{sample} - OD_{CCK-8})}{(OD_{control} - OD_{CCK-8})} * 100\%$$

2.6. Assessment of in vitro sensing performance

The colorimetric response was assessed *in vitro* by applying H_2O_2 solutions (0–1000 μM) to the surface of the Pd-PCN/TMB@MN. After a 20 min reaction, the MN patches were photographed using a smartphone fixed at a distance of 20 cm under standardized 6500 K illumination directed at the patch side. The RGB values of these images were acquired using the ColorAssist app, and the R/(R+G+B) ratio served as the analytical signal for establishing a calibration curve. For reproducibility assessment, eight Pd-PCN/TMB@MN patches from the same batch were inserted into an artificial skin model containing 20 mM H_2O_2. After reaction for 20 min, they were removed, and their RGB values were obtained using the same smartphone method.

2.7. Evaluation in skin models

Potential interference from the skin matrix was evaluated by applying the Pd-PCN/TMB@MN to both normal and H_2O_2-treated *ex vivo* porcine skin, followed by systematic comparison of their colorimetric responses. The tip integrity was also investigated after short-term (20 min) versus prolonged (1, 2, 4 h) application.

To detect the degradation behavior of the integrated MN within the skin and the possible leakage of its loaded components, the skin penetration experiment was carried out using the Franz cells with *ex vivo* porcine skin as the barrier, as previously described by us [10]. The FITC-labeled Pd-PCN@MN patches, with FITC serving as a fluorescent surrogate for TMB, were prepared and applied on the skin. After treatment for a designated time (20 min, 1 h, 2 h, and 4 h), the MNs were removed. The diffusion depth and distribution of both FITC and the intrinsic porphyrin fluorescence from the PCN framework within the skin were visualized using confocal laser scanning microscopy (CLSM, Nikon AXR, Japan). Imaging was performed in dual channels respectively using 488 nm and 561 nm excitation for FITC and porphyrin with a 20 × objective. The acquired optical sections were used for three-dimensional reconstruction to analyze the transdermal penetration profiles.

3. Results and discussion

3.1. Characterization of the Pd-PCN nanoparticle

The structure and composition of the as-prepared Pd-PCN were systematically characterized with different techniques. The SEM image revealed its spherical morphology (Fig. 1a), while the high-resolution TEM image showed the Pd nanoparticles were uniformly distributed throughout the structure with an average size of approximately 5 nm (Fig. 1b). The observed lattice fringe spacing of 0.22 nm (Fig. 1c) corresponded to the (111) crystal plane [19]. Elemental mapping (Fig. 1d) revealed the homogeneous distribution of C, O, Zr, and Pd, providing direct evidence for the successful loading of Pd nanoparticles. The EDS quantitative analysis (Fig. 1e) further confirmed the presence of Pd, showing a characteristic peak with a relative content of 20.48 %. The XRD pattern (Fig. 1f) of Pd-PCN, when compared to that of PCN-224, exhibited additional diffraction peaks corresponding to the (111), (200), (220), and (311) crystal planes of metallic Pd, consistent with the lattice spacing observed in Fig. 1c. In the FT-IR spectra (Fig. 1g), the strong peaks at 1600 cm^{-1} and 1700 cm^{-1} were attributed to C═O stretching vibrations, the peak at 1400 cm^{-1} corresponded to COO– stretching vibrations, and the peak at 700 cm^{-1} was associated with Zr–OH absorption. A slight shift in the characteristic porphyrin ring peak (~1600 cm^{-1}) was observed for Pd-PCN relative to PCN-224, suggesting the possible interaction and coordination with Pd. Notably, the Zr–OH bond vibration showed no significant shift, and no new extraneous peaks emerged. These spectral features confirm the successful synthesis of an intact PCN-224 framework, its stability after Pd loading, and the coordination of Pd with the porphyrin ligands. The above findings collectively demonstrated that Pd incorporation could enhance the dispersion of catalytically active sites within the porous architecture and reinforce the structural stability of the composite, providing a robust platform for sustained catalytic performance [20].

3.2. POD-like activity of the Pd-PCN

Assessed by the catalytic oxidation of TMB with H_2O_2, Pd-PCN exhibited higher absorbance at 652 nm compared to PCN-224 (Fig. 2a), confirming that the enhancement effect was due to the incorporated Pd nanoparticles. Subsequently, the effects of pH, temperature, and H_2O_2 concentration on the catalytic activity of Pd-PCN were investigated. The maximum activity was observed at pH 4.0, as evidenced by the highest absorption (Fig. 2b). The absorption decreased noticeably at pH 5.0, while below pH 4.0, the blue oxidant TMB (oxTMB) became unstable and underwent further oxidation to a yellow diimine derivative [21]. The optimal reaction temperature and H_2O_2 concentration were determined to be 40°C and 1 mM, respectively (Figs. 2c and 2d). At higher temperature, the decreased activity might be caused by accelerated H_2O_2 decomposition [22]. The time-dependent measurements (Fig. 2e) showed a rapid absorption increase specific to Pd-PCN, while both PCN and blank groups remained constant, further demonstrating that its intrinsic POD-like activity of Pd-PCN was attributable to the incorporated Pd nanodots. Thus, the optimal conditions were determined as pH 4.0 and 40°C. For practical skin application, the required acidic environment can be provided locally by an acidic matrix. Although the reaction would be somewhat slower at skin temperature, effective detection could still be achievable within a defined period, which would be verified by our consequent experiment.

The steady-state kinetic assay of Pd-PCN was performed by varying the concentration of one substrate (TMB or H_2O_2) while keeping the other constant. Within a suitable substrate concentration range, the absorption at 652 nm was converted to reaction velocity using the molar extinction coefficient of the oxidized TMB (39,000 $M^{-1}cm^{-1}$). The resulting data were found to fit well to the Michaelis-Menten model, as shown in Figs. 2f and 2g. The Michaelis constant (K_m), an indicator of the enzyme's affinity for its substrate, was obtained using Lineweaver-

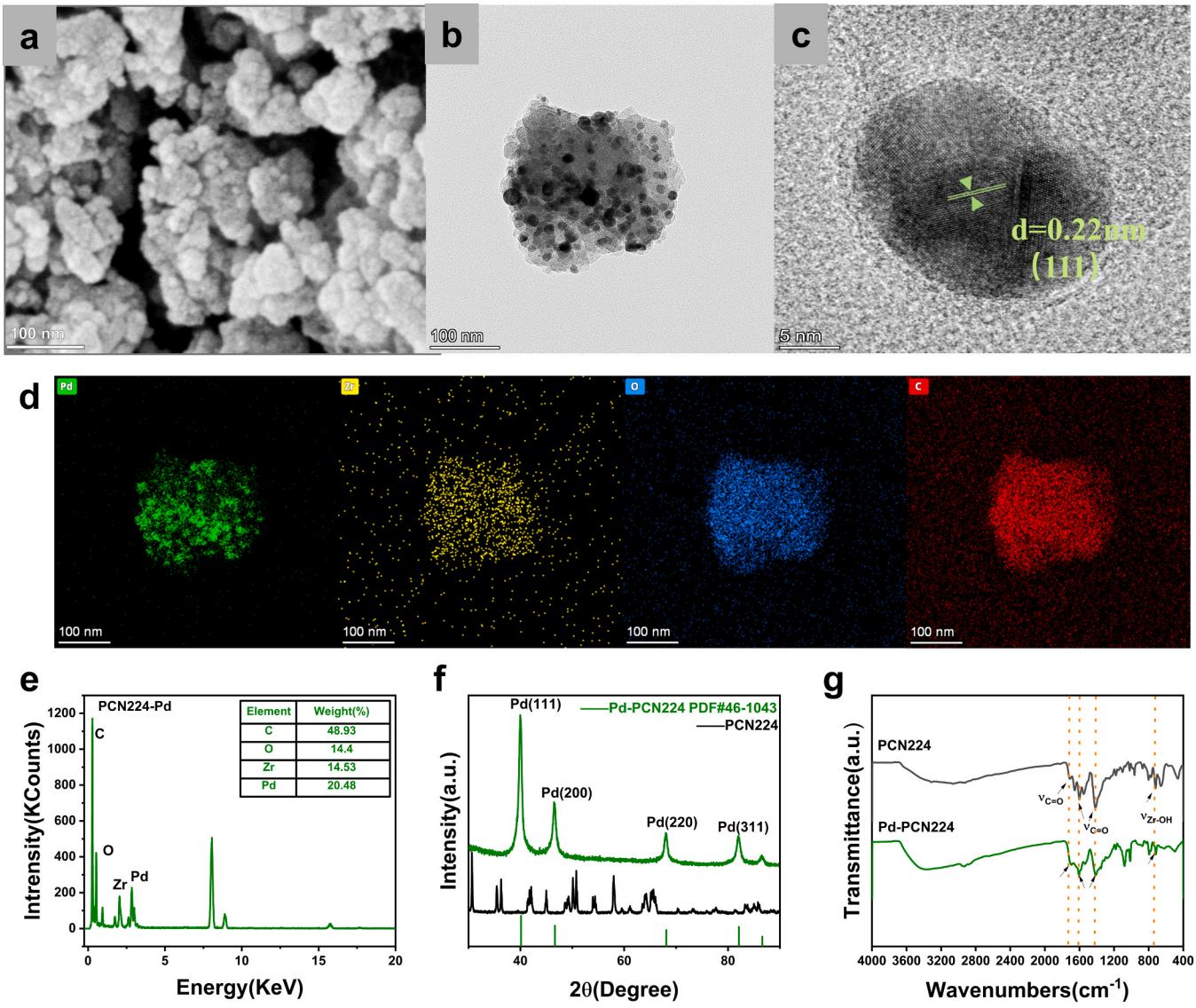

Fig. 1. Structural and compositional characterization of Pd-PCN. (a) SEM image of Pd-PCN. (b) TEM image of Pd-PCN. (c) Lattice diffraction pattern of Pd-PCN. (d) TEM mapping of Pd-PCN. (e) EDS spectrum of Pd-PCN. (f) XRD patterns of PCN-224 and Pd-PCN, and (g) FT-IR spectra of PCN-224 and Pd-PCN.

Burk plot:

$$\frac{1}{v} = \left(\frac{K_m}{V_{max}}\right)\left(\frac{1}{S}\right) + \left(\frac{1}{V_{max}}\right)$$

where v represented the initial velocity, S is the substrate concentration, V_{max} is the maximal reaction velocity, and K_m is the Michaelis constant.

Pd-PCN exhibited K_m values of 0.58 mM for TMB and 10.15 mM for H_2O_2, with corresponding V_{max} values of 21.59 μM·s^{-1} and 10.338 μM·s^{-1} , respectively. These parameters surpass those of most reported nanozymes (Table 1), demonstrating its superior catalytic efficiency and higher substrate affinity [31]. The kinetic parameters obtained in solution reflect the intrinsic peroxidase-mimicking activity of Pd-PCN, a material property that is subsequently harnessed within the solid-state MN by tailoring the local hydrogel microenvironment.

3.3. Stability and interference resistance of Pd-PCN

The batch-to-batch stability was assessed through eight replicate experiments, showing a relative standard deviation (RSD) of 4.24 % (Fig. 2h). This RSD value is below the 5 %, indicating excellent precision and high reproducibility across syntheses. To evaluate the specificity of Pd-PCN towards H_2O_2, interference tests were conducted by introducing common biological substances, including Mg^{2+}, K^+, Ca^{2+}, Na^+, Cl^-, glucose (Glu), glycine (Gly), bovine serum albumin (BSA), and reductive species such as ascorbic acid (AA), glutathione (GSH), uric acid (UA). Under the targeted oxidative stress conditions for the MN sensing, direct reductants (e.g., AA and GSH) are depleted, whereas certain endogenous antioxidant markers like UA may exhibit a compensatory increase [32]. Therefore, these potential reductive interferents were introduced at their corresponding low pathophysiological levels (10 μM for GSH and AA; 200 μM for UA). Based on three independent replicates, the recovery rates for all tested conditions consistently exceeded 90 %, demonstrating strong anti-interference capability and specific responsiveness to the target analyte (Fig. 2i).

3.4. Preparation optimization of Pd-PCN-MN

The matrix composition of the MN patch was systematically optimized to ensure both structural integrity and sensing performance. While PVA served as the primary matrix material, its inherent rigidity could hinder substrate diffusion and reaction kinetics. To modulate this, CS was introduced to soften the matrix and accelerate detection.

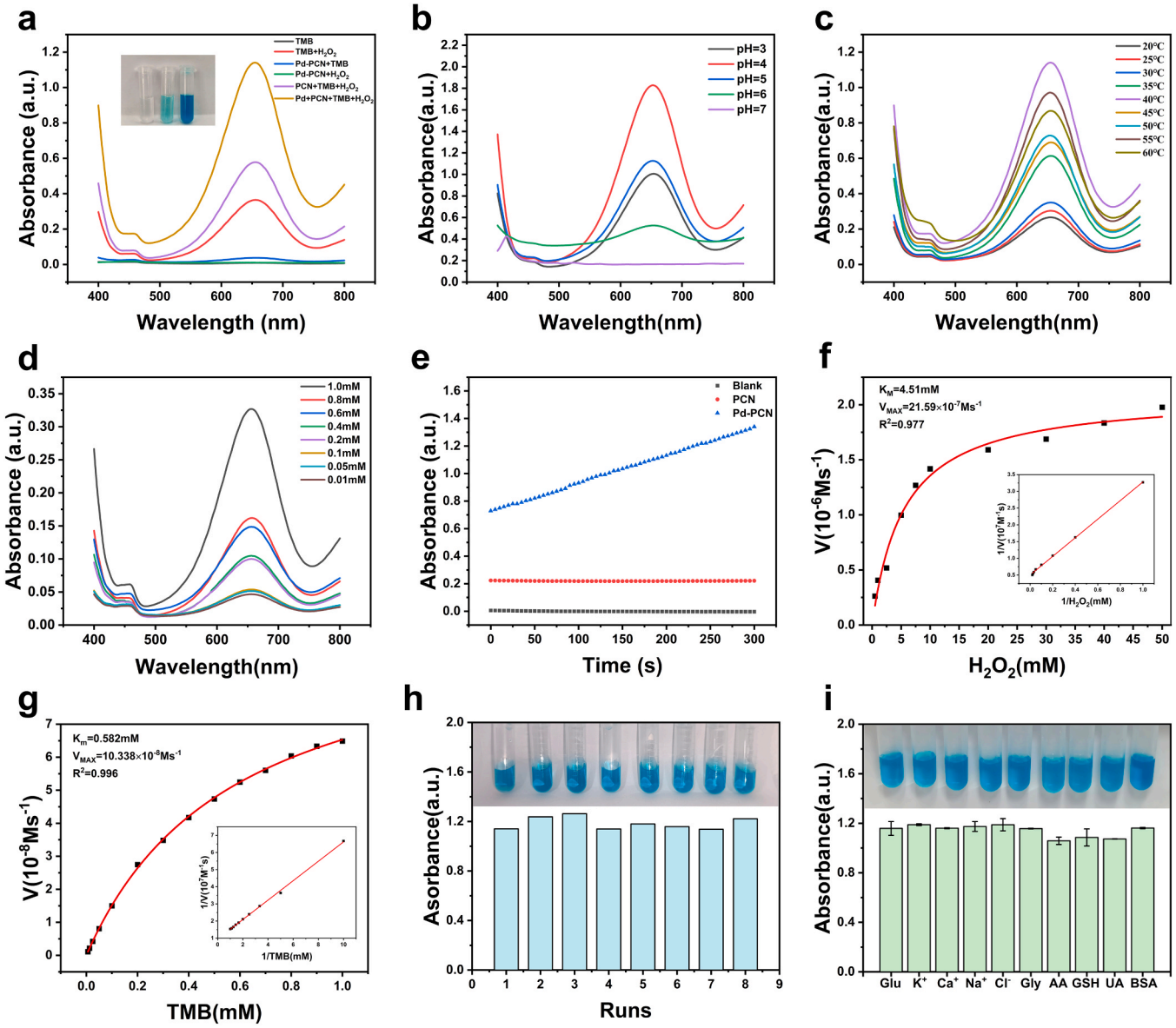

Fig. 2. The POD-like activity of the nanozyme. (a) Typical UV–vis spectrum. Inset: TMB-H_2O_2 solutions (left to right: blank, PCN-224, Pd-PCN) (b) pH Effect. (c) Temperature Effect. (d) H_2O_2 concentration Effect. (e) Time-dependent kinetics. (f, g) Steady-state kinetic assay with varying H_2O_2 or TMB concentration. (h) Stability. i) Interference resistance.

Table 1
Apparent K_m and V_{max} of Pd-PCN and other reported nanozymes for H_2O_2 detection.

Catalyst	K_m(mM)	V_{max}(10^{-7}Ms^{-1})	Ref.
HPR	3.77	0.871	-
Pt-PIL-MWCNTs	16.55	0.7163	[23]
AuNBPs@CuZn	0.47	12.38	[24]
HOF@HRP	6.09	0.468	[25]
$MgFe_2O_4$MNPs	4.61	1.346	[26]
Fe_3O_4/LNPs	5.30	0.096	[27]
Zn-CuO	7.1	0.030	[28]
Cu-Fe_3O_4/Polymer	6.7	0.091	[29]
Pt@ZIF-8	5.27	1.28	[30]
Pd-PCN	4.51	21.59	this work

Morphological screening via optical photograph (Fig. 3a) revealed that MNs fabricated with 10 % PVA exhibited intact needles but a wrinkled backing layer, while 5 % PVA led to tip bending and deformation. In contrast, 7.5 % PVA yielded the optimal needle structure. Functional assessment showed that the composite of 7.5 % PVA with 1 % CS achieved the highest insertion efficiency (Fig. 3b) and needle yield (Fig. 3c). Consequently, 7.5 % PVA with 1 % CS was identified as the optimal matrix composition for subsequent experiments. This matrix was prepared at pH 4.0 to maintain the locally acidic microenvironment required for the optimal POD-like activity of the encapsulated Pd-PCN nanozyme, thereby effectively translating the *in vitro* optimized catalytic conditions to the *in situ* sensing environment within the skin.

The Pd-PCN nanozyme and the TMB chromogen were then co-immobilized within this matrix using a sequential loading process, which layered them to prevent premature mixing and oxidation, thereby enhancing the stability. Upon MN insertion, the absorbed interstitial fluid could swell the hydrogel, enabling controlled diffusion and mixing of the components to ensure the signal specificity and reproducibility. Following this design, the Pd-PCN/TMB@MNs were fabricated and characterized. SEM imaging (Fig. 3d) confirmed a well-ordered array of sharp, conical needles with a height of approximately 600 μm. The force–displacement profiles (Fig. 3e) for both blank MNs (7.5 % PVA + 1 % CS) and Pd-PCN/TMB-loaded MNs displayed a smooth transition

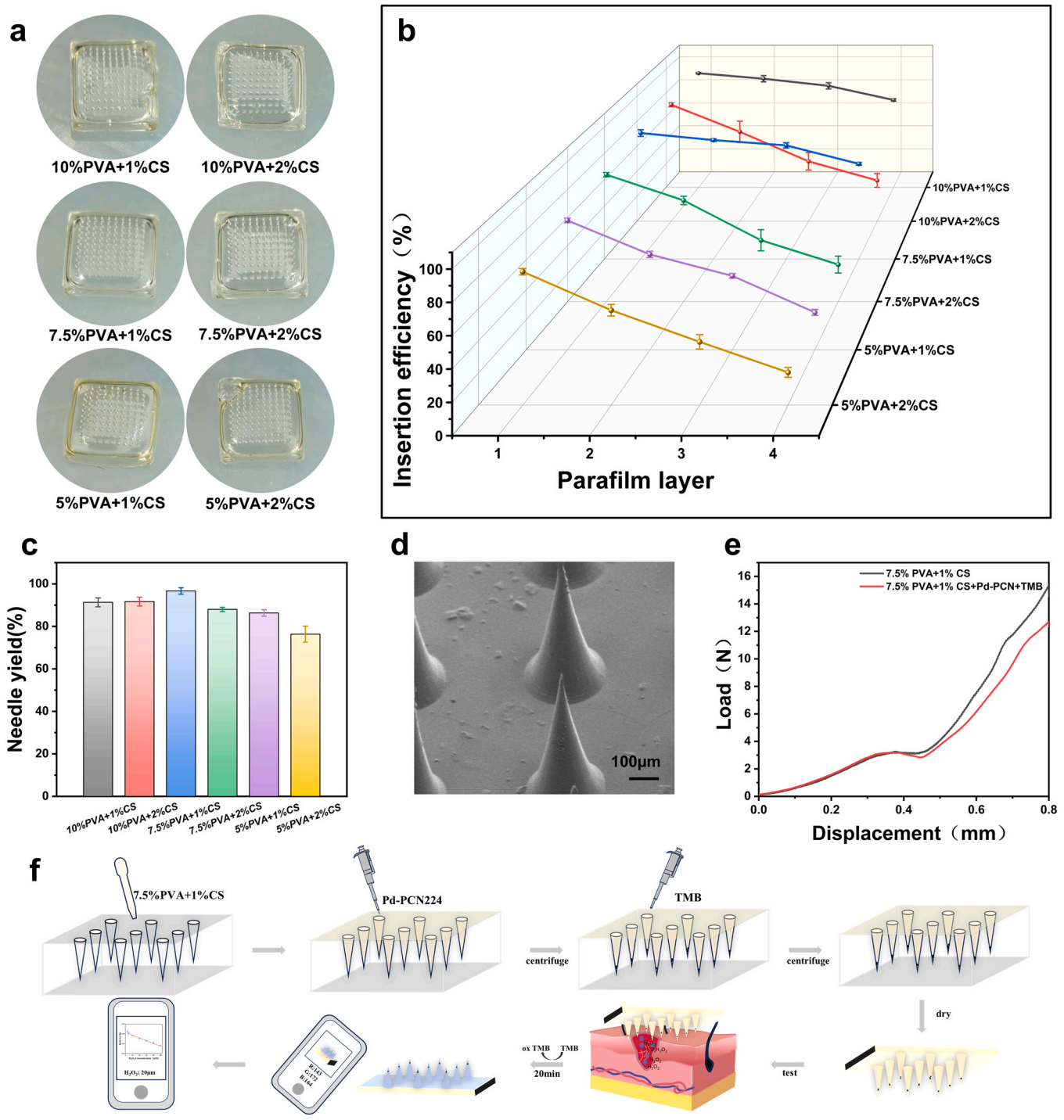

Fig. 3. Preparation and characterization of PCN-Pd/TMB@MN. (a) Optical images. (b) Insertion efficiency. (c) Needle yield. (d) Mechanical property (force-displacement curves). (e) SEM morphology of the optimized MN. (f) Fabrication schematic.

from a linear region to a plateau with reduced slope, without a sharp fracture peak. This behavior indicated progressive plastic deformation, which initiated at a force of 2.5 N, a value substantially exceeding the reported force required to penetrate human skin [33]. The mechanical property was preserved after incorporation of Pd-PCN and TMB into the MN. Thus, the optimized MN formulation, fabricated via the sequential loading process (Fig. 3f), maintained the mechanical robustness necessary for skin penetration, even after incorporating the sensing components.

3.5. Biocompatibility of Pd-PCN/TMB@MN

To evaluate the biocompatibility of the developed nanozyme and MN for direct skin interaction, we employed the well-established HaCaT cell line, as it constitutes over 90 % of epidermal cells [34]. A standard *in vitro* extraction method was applied to the MN patches. As shown in Figs. 4a and 4b, the cell viability consistently exceeded 80 % for both Pd-PCN and Pd-PCN/TMB@MN across all tested concentrations, confirming their good biocompatibility and biosafety.

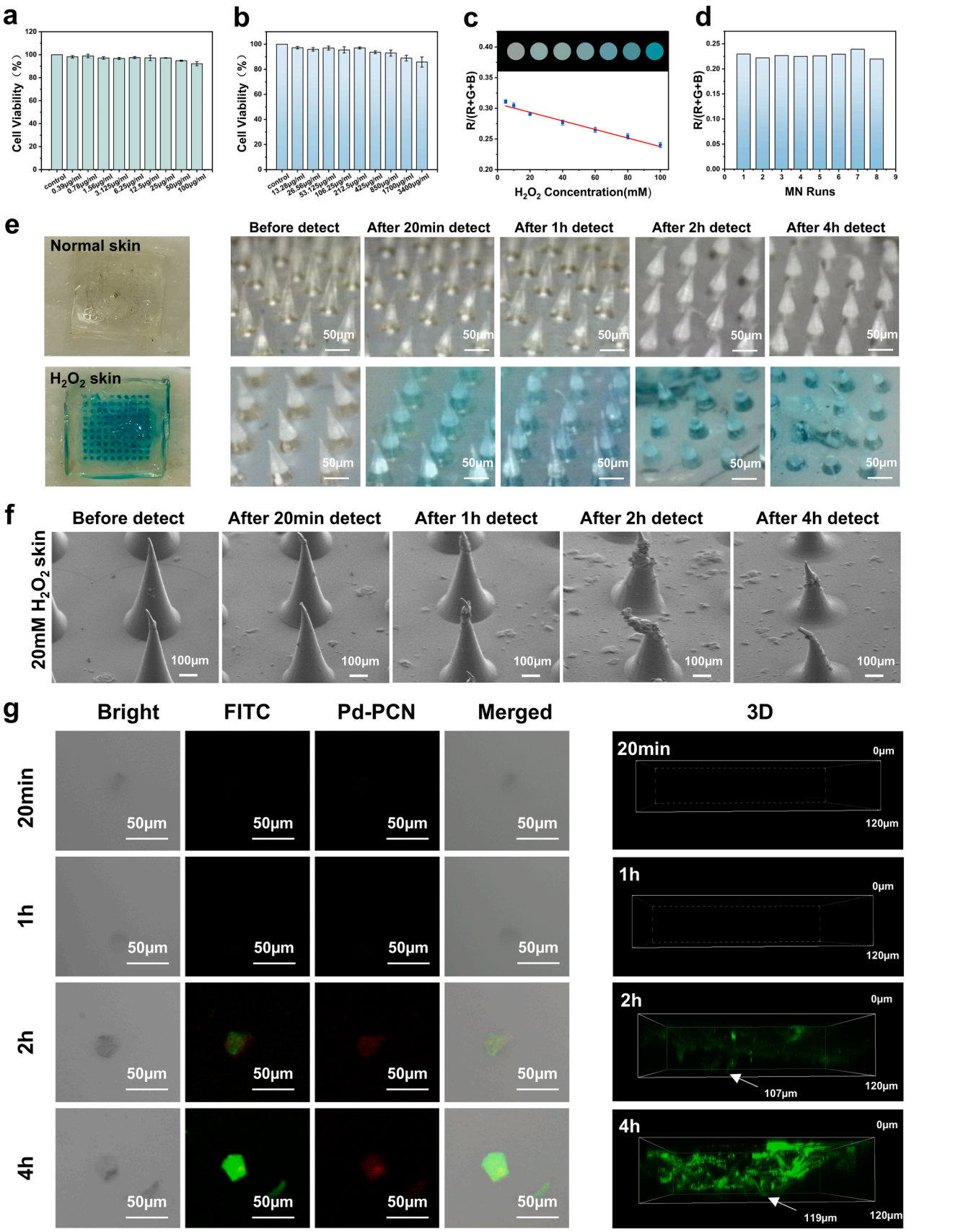

Fig. 4. Application of Pd-PCN/TMB@MN for cutaneous H_2O_2 sensing. (a) Biocompatibility of the PCN-Pd. (b) Biocompatibility of Pd-PCN/TMB-MN. (c) Linear relationship between the R/(R+G+B) ratio and H_2O_2 concentration. (d) Signal reproducibility. (e) Visual response on normal and H_2O_2-treated skin and needle tip integrity over time. (f) Representative SEM images of Pd-PCN/TMB@MN following insertion into H_2O_2-treated skin over time. (g) CLSM images tracking fluorescence distribution in the skin over time.

3.6. Sensing performance of Pd-PCN/TMB@MN

The *in vitro* sensing performance of the Pd-PCN/TMB@MN patch was first evaluated using standard H_2O_2 solutions. As shown in Fig. 4c, a distinct and concentration-dependent blue color developed at the MN tips upon exposure to H_2O_2 from 5 to 100 μM. Quantitative smartphone-based RGB analysis yielded a strong linear correlation ($r = 0.998$) between the normalized red ratio R/(R+G+B) and H_2O_2 concentration. The limit of detection (LOD) was calculated to be 1.53 μM using the formula LOD = 3σ/S, where σ represented the standard deviation of the blank signal (n = 8) and S was the slope of the calibration curve. The basal level of H_2O_2 in healthy skin interstitial fluid is typically maintained in the nanomolar to low micromolar range. However, under pathological conditions such as vitiligo, its concentration can rise significantly into the tens of micromolar range [2]. Our developed colorimetric MN sensor, with a linear detection range of 5–100 μM, is well-suited to capture these disease-relevant elevations. An advantage of our sensor is its lower limit of detection (5 μM), which is notably superior to a reported wearable sweat sensor based on laser-induced graphene (linear range: 10–1000 μM) [35]. While another wearable MN sensor utilizing a Prussian blue-carbon nanotube composite electrode reports a lower detection limit (1–10 μM) [18], our colorimetric platform offers the distinct practical advantage of easy use and accessibility, making it particularly suitable for point-of-care application.

The reproducibility of the Pd-PCN/TMB@MN was assessed by testing eight MN patches from the same fabrication batch at a fixed H_2O_2 concentration. As shown in Fig. 4d, the mean R/(R+G+B) ratio had a SD of 0.227 and a RSD of 2.62 %, indicating acceptable precision and reproducibility. Matrix interference from skin tissue was tested by comparing the colorimetric response on normal versus H_2O_2-treated skin. As shown in Fig. 4e, a distinct colorimetric signal was observed only on the H_2O_2-treated skin, demonstrating that normal skin components did not interfere the detection and thus validating the sensing specificity. The water-absorbing capacity of the MN patch was quantified gravimetrically after skin insertion, showing an uptake of 4.28 ± 0.52 μL of interstitial fluid per patch. This volume provided an aqueous microenvironment sufficient for the nanozyme-catalyzed reaction, as confirmed by the distinct colorimetric signal generated on H_2O_2-treated skin.

Furthermore, we monitored both the colorimetric signal and the morphological stability of Pd-PCN/TMB@MN needle tips over time to evaluate performance and potential degradation in the skin. The signal intensity reached a plateau within the standard 20-min assay and did not increase with prolonged residence time up to 1 or 2 h. Morphologically, the needle tips maintained complete integrity in normal skin over prolonged periods and in H_2O_2-treated skin for up to 1 h. However, tip bending and partial degradation became evident after 2–4 h of exposure in H_2O_2-treated skin (Fig. 4e), with SEM images clearly showing a progressive reduction in needle dimensions over time (Fig. 4f). These findings collectively validated the operational safety and analytical reliability of Pd-PCN/TMB@MN under its intended short-term detection conditions.

The dual-fluorescence MN patch, co-loaded with the intrinsically fluorescent PCN skeleton and FITC (as a TMB surrogate), was used to simultaneously track the in-skin integrity and distribution of the nanozyme carrier and the chromogen from the MN into the skin. Confocal microscopy (Fig. 4g) revealed no green fluorescence from FITC or red fluorescence from the Pd-PCN nanoparticles at 20 min or 1 h, indicating no content release. At 2 h, the emergence and diffusion of both signals indicated the onset of matrix dissolution and content release, which progressed further by 4 h. These results confirmed that this MN platform could function as a session-lasting system, maintaining full structural integrity within the intended short-term monitoring window, thus ensuring reliable signal readout and minimizing the risk of introducing exogenous substances into the skin.

Building on this structural stability, the biosafety of the Pd-PCN/TMB@MN patch is fully ensured. First, the "session-lasting" hydrogel matrix acts as a physical barrier to minimize component exposure during use. Second, even if released, the intrinsic biocompatibility of these key components, as validated by the cytotoxicity assessment, would provide an additional safety guarantee. Collectively, these attributes establish the developed MN as a safe device for skin monitoring.

4. Conclusion

This study established an integrated smartphone and nanozyme-based MN platform for in situ H_2O_2 detection in the skin. The system employed a stable hydrogel matrix that integrated the Pd-PCN nanozyme with the chromogenic substrate TMB, enabling minimally invasive sampling, a contained reaction microenvironment, and session-lasting structural integrity. It demonstrates robust analytical performance, biosafety, and in-skin stability. This work addresses the challenge of monitoring oxidative biomarkers in skin tissue by establishing an integrated platform that combines nanozyme catalysis, sensing technology, and smartphone-based readout for point-of-care diagnostics. To facilitate patient adoption, the system can be enhanced with clear instructions and visual color guides, holding significant potential for personalized management of dermatological diseases such as chronic wounds, and inflammatory skin disorders.

CRediT authorship contribution statement

Meng Sun: Investigation, Data curation. **Feng Liu:** Writing – original draft, Investigation. **Lei Yang:** Writing – review & editing, Methodology. **Hongchun Gu:** Investigation. **Yang Chen:** Writing – review & editing, Project administration, Conceptualization. **Xun Feng:** Methodology, Funding acquisition, Conceptualization. **Sihui Wang:** Writing – original draft, Investigation, Data curation.

Funding

This work was supported by the Science Research Foundation of Education Department for Liaoning Province (LJ212510164025).

Declaration of Competing Interest

The authors declare that they have no known competing financial interests or personal relationships that could have appeared to influence the work reported in this paper.

Data availability

Data will be made available on request.

References

[1] E.C. Murphy, A.J. Friedman, Hydrogen peroxide and cutaneous biology: translational applications, benefits, and risks, J. Am. Acad. Dermatol. 81 (2019) 1379–1386.
[2] S. Jankovskaja, A. Labrousse, L. Prévaud, B. Holmqvist, A. Brinte, J. Engblom, M. Rezeli, G. Marko-Varga, T. Ruzgas, Visualisation of H_2O_2 penetration through skin indicates the importance to develop pathway-specific epidermal sensing, Mikrochim. Acta 187 (2020) 656.
[3] M. Zhou, H. Sun, S. Chen, M. Yang, R. Dong, X. Yang, L. Zang, Chemosensors for H_2O_2 detection: principles, active materials, and applications, Chemosensors 13 (2025) 54.
[4] X. Li, Y. Zhang, Z. Chen, Recent progress of nanozyme-based sensors in point-of-care testing, smartphone-integrated nanozyme approaches for rapid and on-site detection: empowering smart food safety, ACS Sens. 8 (2023) 1800–1820.
[5] Y. Zhou, T. Luan, Q. Fang, Y. Zhang, Y. Du, Molecularly tailored Pd@Pt nanozymes for real-time smartphone-assisted acetylcholinesterase detection and therapeutic inhibitor assessment, Sens. Actuators B Chem. 440 (2025) 137889.
[6] M. Lian, F. Shi, Q. Cao, C. Wang, N. Li, X. Li, X. Zhang, D. Chen, Paper-based colorimetric sensor using bimetallic Nickel-Cobalt selenides nanozyme with artificial neural network-assisted for detection of H_2O_2 on smartphone, Spectrochim. Acta A. Mol. Biomol. Spectrosc. 311 (2024) 124038.

[7] A. Deshwal, R.M. Tripathi, Palladium-powered nanozymes: a paradigm shift in precision medicine, Chem. Eng. J. 522 (2025) 168043.
[8] R. Dadigala, R. Bandi, M. Alle, C.W. Park, S.Y. Han, K. G.J, S.H. Lee, Effective fabrication of cellulose nanofibrils supported Pd nanoparticles as a novel nanozyme with peroxidase and oxidase-like activities for efficient dye degradation, J. Hazard. Mater. 436 (2022) 129165.
[9] X. Sun, X. Chen, S. Wang, H. Gu, H. Bao, Z. Ning, X. Feng, Y. Chen, Oxygenous and biofilm-targeted nanosonosensitizer anchored with Pt nanozyme and antimicrobial peptide in the gelatin/sodium alginate hydrogel for infected diabetic wound healing, Int. J. Biol. Macromol. 923 (2025) 139356.
[10] X. Sun, Q. Wang, H. Bao, Y. Liu, S. Yao, M. Li, N. Chen, Y. ChenPorphyrinic metal-organic framework PCN-224 nanoparticles for colocalization of nanoparticle-cargo in the skin and enhancement of sonodynamic efficacyACS. Appl. Nano. Mater.72022614-2629.
[11] F. Rastgoo, F. Amourizi, K. Dashtian, R. Zare-Dorabei, M. Mahdavi, M. Noroozifar, K. Kerman, Visual point-of-care diabetic breath diagnosis with integration of dye/MOF on permeable hydrophilic polypropylene fabric, Microchem. J. 216 (2025) 114605.
[12] F. Amourizi, K. Dashtian, R. Zare-Dorabei, S. Hajati, Transformative personalized oxalate biomarker analysis through a wrist-worn microneedle device integrated with duplex nanozyme toolbox, Sens. Actuators B. Chem. 423 (2025) 136731.
[13] Y. Wei, W. You, H. Li, J. Chen, Z. Tang, Y. Luo, W. Xiao, Q. Yang, M. Feng, L. Li, M. Wang, Stimuli-responsive nanozymes for wound healing: from design strategies to therapeutic advances, Mater. Today Bio 33 (2025) 102046.
[14] R. Li, Z. Liu, Y. Xiong, X. Zhang, L. Chen, D. Li, C. Huang, S. Yu, X. Jia, A smartphone-enabled colorimetric microneedle sensing platform for rapid detection of ascorbic acid in fruits, ACS Appl. Mater. Interfaces 16 (2024) 63941–63950.
[15] X. Li, J. Lv, J. Zhao, G. Ling, P. Zhang, Swellable colorimetric microneedles for glucose detection based on glucose oxidase-like gold nanoparticles, Anal. Chim. Acta 1288 (2024) 342152.
[16] E. Chen, P. Chang, H. Xu, H. Xu, Z. Zhu, D. Shen, Integrated colorisensing platform with microneedles and metal-phenol nanozymes for point-of-care testings of acetylcholinesterase activity and its drug inhibitor, Int. J. Nanomed. 20 (2025) 14629–14642.
[17] W. Wang, R. Feng, K. Wei, J. Xu, W. Dong, J. Li, J. Sun, S. Wang, X. Mao, An integrated colorimetric biosensing platform containing microneedle patches and aptasensor for histamine monitoring in seafood, J. Hazard. Mater. 489 (2025) 137536.
[18] J. Zhu, L. Wang, S. Xu, L. Peng, Z. Gao, S. Liu, S. Xi, S. Ma, W. Cai, A high-performance wearable microneedle sensor based on a prussian blue-carbon nanotube composite electrode for the detection of hydrogen peroxide and glucose, Sens. Actuators B. Chem. 419 (2024) 136436.
[19] K. Singh, K.K. Maurya, M. Malviya, Electrochemical determination of dopamine using Ni Pd bimetallic nanoparticles decorated on MWCNT: an amperometric sensor, J. Nanopart. Res. 26 (2024) 63.
[20] C. Chen, Q. Mo, Y. Wang, L. Zhang, Cooperative catalytic alkyne hydrosilylation by a porphyrinic metal-organic framework composite, Inorg. Chem. 62 (2023) 16882–16889.
[21] V.G. Panferov, N.A. Byzova, A.V. Zherdev, B.B. Dzantiev, Peroxidase-mimicking nanozyme with surface-dispersed Pt atoms for the colorimetric lateral flow immunoassay of C-reactive protein, Microchim. Acta 188 (2021) 309.
[22] F. Sun, C.X. Xie, F. Zhang, M.P. Jin, Z.G. Wang, Effect of pH on the adiabatic decomposition characteristics of hydrogen peroxide, Chem. Eng. (China). 40 (2012) 42–45.
[23] L. Gong, Y. Chen, X. Bai, T. Xu, S. Wu, W. Song, X. FengPeroxidase-mimicking Pt nanodots supported on polymerized ionic liquid wrapped multi-walled carbon nanotubes for colorimetric detection of hydrogen peroxide and glucoseMicrochem J.202, 105872 .
[24] M. Wang, F. Shi, J. Li, L. Min, Z. Yang, J. Li, An Au bipyramids@CuZn MOF core-shell nanozyme enables universal SERS and a colorimetric dual-model bioassay, Chem. Commun. 60 (2024) 6019–6022.
[25] G. Chen, M. Sha, W. Xu, M. Xu, Y. Chen, C. Zou, H. Ye, C. Zhu, W. Gu, Protein-directed hydrogen-bonded organic framework with enhanced enzyme stability and catalytic efficiency for sensitive colorimetric/fluorometric immunoassays, Sens. Actuators B Chem. 405 (2024) 135347.
[26] L. Su, W. Qin, H. Zhang, et al., The peroxidase/catalase-like activities of MFe2O4 (M=Mg, Ni, Cu) MNPs and their application in colorimetric biosensing of glucose, Biosens. Bioelectron. 63 (2015) 384–391, https://doi.org/10.1016/j.bios.2014.07.048.
[27] Q. Zhang, M. Li, C. Guo, Z. Jia, G. Wan, S. Wang, D. Min, Fe3O4 nanoparticles loaded on lignin nanoparticles applied as a peroxidase mimic for the sensitively colorimetric detection of H2O2, Nanomaterials (2019).
[28] A.P. Nagvenkar, A. Gedanken, Cu0.89Zn0.11O, a new peroxidase-mimicking nanozyme with high sensitivity for glucose and antioxidant detection, ACS Appl. Mater. Interfaces 8 (2016) 22301–22308.
[29] T. Zhang, X. Qu, S. Sun, Z. Zhang, Y. Qiu, P. Wu, P. Ding, Engineering Cu-Fe3O4/polymer dots hybrids for dual-mode detection of chlortetracycline, recognition-enhanced water pollutant degradation, and bacterial disinfection, Small 21 (2025) e2501187.
[30] B. Shen, Q. Wu, Y. Guo, J. Qin, H. Chen, Y. Yang, Z. Liu, L. Li, W. Li, C. Zhu, Modulating the hydrophilic-hydrophobic microenvironment of MOF-stabilized Pt nanozymes: the role of H_2O in the peroxidase-like catalyzed reaction, Adv. Funct. Mater. 35 (2024) 2415854.
[31] L. Jiang, S. Li, M. Deng, W. Hu, C. Lü, Metal-organic frameworks (MOFs) wrapped palladium nanoparticles-loaded Fe_3O_4@CFR core-shell magnetic nanohybrid as heterogeneous catalyst with robust catalytic properties, Colloid Surf. A 694 (2024) 134171.
[32] P.A. Hirt, Y. Umasankar, P. Bhushan, L. Borda, S. McNamara, C. Chen, F. MacQuhae, B. Shekhar, K. Robert, H. Lev-Tov, Uric acid levels in chronic wounds are elevated compared with adjacent normal skin, J. Am. Acad. Dermatol. 81 (1) (2019). AB143.
[33] L. Piccolo, K. Bornillo, S. Micheli, M. Sorgato, M. Ricotta, E. Cimetta, G. Lucchetta, A penetration efficiency model for the optimization of solid conical microneedles' geometry, J. Micromech. Microeng. 34 (2024) 025009.
[34] E.P. Yalcintas, D.S. Ackerman, E. Korkmaz, C.A. Telmer, J.W. Jarvik, P. G. Campbell, M.P. Bruchez, O.B. Ozdoganlar, Analysis of in vitro cytotoxicity of carbohydrate-based materials used for dissolvable microneedle arrays, Pharm. Res. 37 (2020) 33.
[35] R. Barber, J. Davis, P. Papakonstantinou, Stable chitosan and prussian blue-coated laser-induced graphene skin sensor for the electrochemical detection of hydrogen peroxide in sweat, ACS Appl. Nano Mater. 6 (2023) 10290–10302.

Yang Chen is an associate Professor in China Medical University. He received his BSc and PhD degrees in Pharmaceutics from Shenyang Pharmaceutical University in 2009 and 2014, respectively. In 2023, he worked as a visiting scholar at Aarhus University for one year. His research interests include theranostic system development, tissue engineering, and in vivo biosensing. He has over 30 publications in these areas, wherein almost 20 journal papers have been published as the first or corresponding author.